Materials Advances

ROYAL SOCIETY OF CHEMISTRY

PAPER

View Article Online
View Journal | View Issue

Check for updates

Cite this: *Mater. Adv.*, 2024, 5, 6469

Crystallization kinetics of stacked phase-change films for multi-level storage

Yimin Chen, *[abc] Ce Fan,[ab] Nan Han,[ab] Kexing Peng,[ac] Chenjie Gu,[abc] Zijun Liu,[ac] Guoxiang Wang,[ac] Tiefeng Xu,[ac] Junqiang Wang[d] and Xiang Shen *[ac]

Received 22nd April 2024,
Accepted 4th July 2024

DOI: 10.1039/d4ma00416g

rsc.li/materials-advances

Good thermal stability, fast operation speed, high-level storage density, and low power consumption are increasingly required for neuro-inspired phase-change random access memory. Herein, we designed a multi-level storage phase-change film with three Sb–GeO_2 components that are stacked and separated by SiO_2 dielectric layers. The fragile-to-strong (F–S) kinetics feature, which is desirable in phase-change supercooled liquids for alleviating the contradictory relation between good thermal stability near the glass transition temperature and fast crystallization speed around the melting temperature, is revealed in some of the Sb–GeO_2 components. Moreover, we found that the introduction of stacked structures and adjacent phase-change layers can significantly weaken the F–S kinetics feature of the low thermally stable Sb–GeO_2 film but has no influence on the high thermally stable Sb–GeO_2 film. It is confirmed that the residual stresses arise from the expansion of stacked films are the origins for the influence on the crystallization kinetics. These findings open opportunities for the design of high-density storage devices with multilayer phase-change films to large-scale neuro-inspired computing.

1. Introduction

The increased need for data storage and information processing drives the urgent search for new computing devices. Phase-change random access memory (PCRAM) is an emerging technology, which, unlike flash memory, does not suffer from problems associated with the storage of charge. In comparison with other memories such as dynamic random access memory (DRAM), PCRAM offers a wider range of advantages including superb scalability,[1] faster write/read speed,[2] lower energy consumption,[3] longer data retention time and non-volatility.[4] The above-mentioned advantages of PCRAM are determined by the properties of phase-change materials (PCMs), which show the rapid transition capacity of amorphous to crystalline state with the significant changes in their electrical and/or optical contrast.[5]

Several studies have focused on the improvement of the above-mentioned properties; however, another important characteristic of memory, the storage density, is less investigated. As we noted, both the dimensional down-scaling and the way more akin to "high-rise building" may be supposed eventually to reach the physical limit.[6] Therefore, the concept of multi-stage PCMs, which can realize multiple storage states that provides engineers with an alternative solution to enhance the storage density of monolithic hardware, is proposed. Actually, the flagship Ge–Sb–Te (GST) material undergoes two transitions from amorphous to fcc crystalline structure and fcc to hcp crystalline structure and across three states from high, intermediate, and low resistance, respectively, upon annealing, implying a multistage property.[7] Nevertheless, the narrow temperature span of the intermediate state and high changeable rate of resistance make the control of intermediate resistance state difficult, and the resolution for the data collection is rather low. It was reported that nitrogen doping induces a wide quasi-platform of the intermediate resistance state and simultaneously increases the crystallization temperature due to changes in the electrical structures.[8] Although such a doping method is a universal means to realize multistage function in PCRAM, it easily results in phase separation, which would deteriorate the duration of the memory. Recently, the concept of superlattice method was employed to realize multistage PCMs, such as the GaSb/Ge_2Te,[9] GeTe/Sb_2Te_3,[10] $SnSb_4$–GeTe,[11] GeTe/Ge_8Sb_{92},[12] and SbSe/Ga_3Sb_7.[13] However, two phase-change layers in such superlattice-like PCMs are easy to

[a] *Laboratory of Infrared Material and Devices & Key Laboratory of Photoelectric Materials and Devices of Zhejiang Province, Advanced Technology Research Institute, Ningbo University, Ningbo, 315211, China. E-mail: chenyimin@nbu.edu.cn, shenxiang@nbu.edu.cn*
[b] *Department of Microelectronic Science and Engineering, School of Physical Science and Technology, Ningbo University, Ningbo, 315211, China*
[c] *Engineering Research Center for Advanced Infrared Photoelectric Materials and Devices of Zhejiang Province, Ningbo University, Ningbo 315211, China*
[d] *CAS Key Laboratory of Magnetic Materials and Devices & Zhejiang Province Key Laboratory of Magnetic Materials and Application Technology, Ningbo Institute of Materials Technology & Engineering, Chinese Academy of Sciences, Ningbo, 315201, China*

penetrate, resulting in the functional instability of the multilayer interface.[14]

There are numerous studies on the basic physical characteristics of multilevel storage materials and the fundamental test performance of devices,[15,16] and it suggests that the introduction of dielectric layer (like the SiO_2) to separate the two phase-change layers is helpful to improve the stability of the multilayer interface and the durability of multi-storage PCRAM. Nevertheless, the introduction of a dielectric layer that results in the stacked structure would affect the crystallization kinetics of multilayer PCMs. Especially, the effect of an adjacent PCM layer is rarely mentioned, and there is no systematic investigation to discuss such a significant issue. In this work, we design three nanocomposite Sb–GeO_2 films, which have no phase separation before crystallization and stack them to form a multilayer PCMs that can be used to realize two-bit function in one storage cell with a wide temperature span and stable resistance of each intermediate state. Moreover, together with flash differential scanning calorimetry (FDSC) and generalized Mauro–Yue–Ellison–Gupta–Allan (g-MYEGA) viscosity model, the fragile-to-strong transition (FST) behaviors in Sb–GeO_2 materials were revealed, and the effects of the adjacent phase-change layer on the crystallization kinetics of multilayer PCMs were quantitatively studied.

2. Experimental methods

2.1 Film depositions and characterizations

The single and multilayer Sb–GeO_2 films were deposited on Si(100) and NaCl(100) substrates by magnetron sputtering at room temperature. The high purity Sb (99.95 at%) and GeO_2 (99.95 at%) targets were used to deposit the phase-change layer of Sb–GeO_2, and high purity SiO_2 (99.999 at%) target was employed to deposit the dielectric layer (non-phase-change layer) of SiO_2. The sputtering atmosphere was Ar with a gas flow of 15 sccm. The base pressure was 6×10^{-6} Pa and the working pressure was 3 mT. The compositions of three single Sb–GeO_2 films were *in situ* controlled by the sputtering power of Sb and GeO_2 targets and *ex situ* examined by energy dispersive spectroscopy (EDS, Tescan Vega 3SBH), such as $Sb_{89.2}(GeO_2)_{10.8}$ (the abbreviation is SGO1), $Sb_{72.6}(GeO_2)_{27.4}$ (SGO2), and $Sb_{61.8}(GeO_2)_{38.2}$ (SGO3). Noteworthily, 5 nm-thick SiO_2 layers were also deposited on the two sides of these single Sb–GeO_2 films. With the same sputtering parameters, multilayer Sb–GeO_2 film, which consists of three single film layers and four 5 nm thick SiO_2 layers, were deposited, and its abbreviation is SGO multilayer film. The thickness of each SGO-*X* (X = 1, 2, 3) layer in the SGO multilayer were *in situ* controlled by the deposition time and *ex situ* examined by scanning electron microscopy (SEM). We designed three thickness of 20, 100, and 200 nm for each SGO layer, and the SEM pattern of the typical 100 nm-thick SGO film is shown in Fig. 1. The sheet resistance–temperature (or resistance–time) curves were characterized *via* a homemade heating platform with an accuracy of ±0.1 °C. Three SGO single films and SGO multilayer film

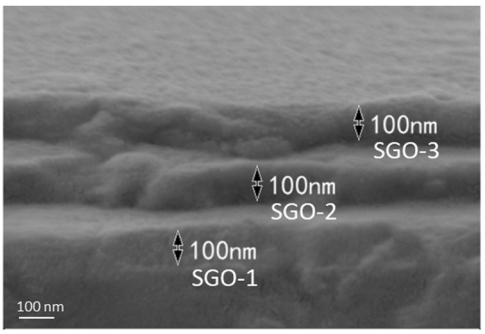

Fig. 1 Cross-sectional view of the SGO multilayer film. The thickness of each SGO phase-change layer is ~100 nm and the dielectric layer SiO_2 is ~5 nm. Although the 5 nm-thick SiO_2 layer cannot be observed from the SEM pattern directly due to the limited maximum resolution, it can be estimated from the total thickness of this multilayer film.

were all annealed in a rapid annealing furnace that was filled with high purity N_2 atmosphere at different temperatures for a holding time of 3 min. The micro-structures of crystalline SGO films were examined by X-ray diffraction (XRD, Bruker D2 PHASER diffractometer, Cu Kα radiation with a wavelength of 0.15405 nm). It should be noted that the XRD patterns of SGO-1, SGO-2, and SGO-3 layer were measured *via* the 170 °C-annealed, 220 °C-annealed, and 270 °C-annealed stacked SGO films, respectively.

2.2 Crystallization kinetics analyses

The peak temperature (T_p) values for crystallization were measured by flash differential scanning calorimetry (FDSC, Mettler Toledo Flash DSC1) at varying heating rates in the range of 20–40 000 K s^{-1}. In order to obtain the reproducible results, all the FDSC measurements were repeated more than 3–5 times at each heating rate both for multilayer and single SGO films. The measurement details are similar to our previous report.[17] Temperature calibration was performed and thermal lag was evaluated before the FDSC measurements in this work. Depending on the measured T_p values and combined with the g-MYEGA viscosity model[18] and Johnson–Mehl–Avrami (JMA) crystallization kinetics model,[19–22] we then studied the crystallization kinetics of single and multilayer SGO films.

3. Results

3.1 Thermal stability and crystallization behavior

Fig. 2(a) shows the resistance–temperature curves of the SGO multilayer phase-change films with different layer thickness of 20 (SGO-20), 100 (SGO-100), and 200 nm (SGO-200). It was found that the sheet resistance suffers from abrupt drops with the boosted temperature, which corresponds to the phase transitions. These multilayer SGO films all undergo three-step phase transition, and this transition seems to become more obvious with the decrease in thickness. By testing the time-dependent resistance of the film at a specific temperature over a period of time, another important parameter, the resistance

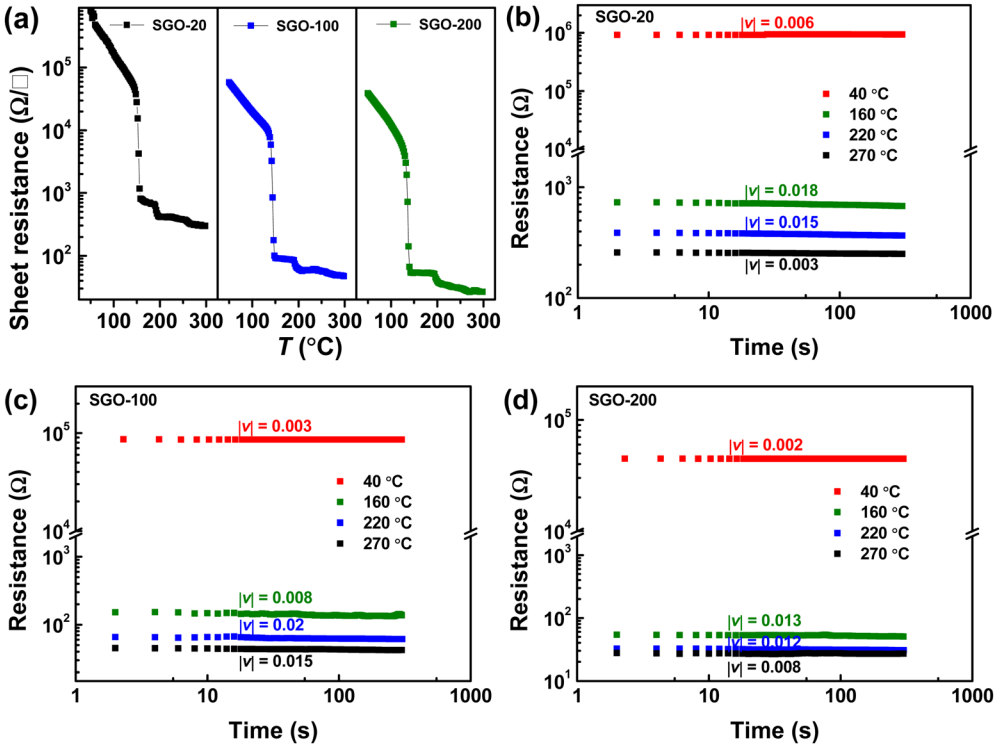

Fig. 2 (a) The temperature-dependent sheet resistances of multilayer SGO films with different PCM layer thickness of 20, 100, and 200 nm. The heating rate is 60 K min^{-1}. The time-dependent sheet resistance of (b) SGO-20, (c) SGO-100, and (d) SGO-200 multilayer films. The annealing temperatures are 40, 160, 220, and 270 °C to determine the resistance drift of amorphous state, first phase transition state (SGO1 crystallized), second phase transition state (SGO2 crystallized), and crystalline state (SGO3 crystallized), respectively.

drift coefficient, can be evaluated by the following formula[23]

$$R(t) = R_0\left(\frac{t}{t_0}\right)^{\nu} \quad (1)$$

where ν is the drift coefficient, t_0 is the initial time (2 s is used here), R_0 is the initial resistance at t_0, and R is the resistance at any time t after the initial time. Fig. 2(b)–(d) show the resistance drift curves of different multilayer SGO films obtained at 40, 160, 220, and 280 °C. As we can see, the ν values of these multilayer SGO films are all smaller than that of the GST film (~0.1). Moreover, the resistance ratio of two intermediate states in the SGO-100 and SGO-20 films are larger than that in the SGO-200 film, indicating the better signal-noise ratio in thinner films. Considering that the 20 nm thick phase-change layer could not meet the sample weight for the FDSC measurement, we thus employed the multilayer SGO film with each phase-change layer of 100 nm for further crystallization kinetics investigation.

Fig. 3(a) shows the temperature-dependent sheet resistance of single SGO films and multilayer SGO (SGO-100) film with a heating rate of 60 K min^{-1}. As we can see, only one phase transition occurs in these SGO single films, and the crystallization temperatures of SGO1, SGO2, and SGO3 are 156, 198, and 250 °C, respectively. For the multilayer SGO film, the three-step phase transition temperatures are 144, 192, and 251 °C. It indicates that the thermal stability of the SGO layer with lower crystallization temperature is more easily influenced by the adjacent phase-change layer in the multilayer SGO film. We further estimated the activation energy for crystallization (E_a) and extrapolated the temperature that data can be stored safely for 10 years (T_{10yr}) using the Arrhenius plot, which is described as:[24]

$$t = \tau \exp(E_a/k_B T) \quad (2)$$

where τ is a proportional time constant and k_B is the Boltzmann constant. The failure time t is defined as the time when the sheet resistance decreases to half of the initial value at a specific temperature T. According to the Arrhenius plots shown in Fig. 3(b), the extrapolated T_{10yr} is 53.8, 91.9, and 146.2 °C with the E_a of 2.16, 2.49, and 3.28 eV, for SGO1, SGO2, and SGO3 films, respectively. Another non-isothermal method named Kissinger plot was carried out to evaluate the crystallization activation energy (Q) of each phase transition in the multilayer SGO film. It is described as:[25]

$$\frac{Q}{R} = -\frac{\mathrm{d}\ln(\Phi/T_p^2)}{\mathrm{d}(1/T_p)} \quad (3)$$

where R is the gas constant, Φ is the heating rate, and T_p is the peak temperature for crystallization. Fig. 3(c) shows the Kissinger plots where the T_p data are determined by the resistance–temperature curves at different heating rates of 10, 20, 40, and 60 K min^{-1}. It yields that the activation energy Q is 1.04, 2.33, and 3.37 eV for the first phase transition (SGO-1), second phase transition (SGO-2), and third phase transition

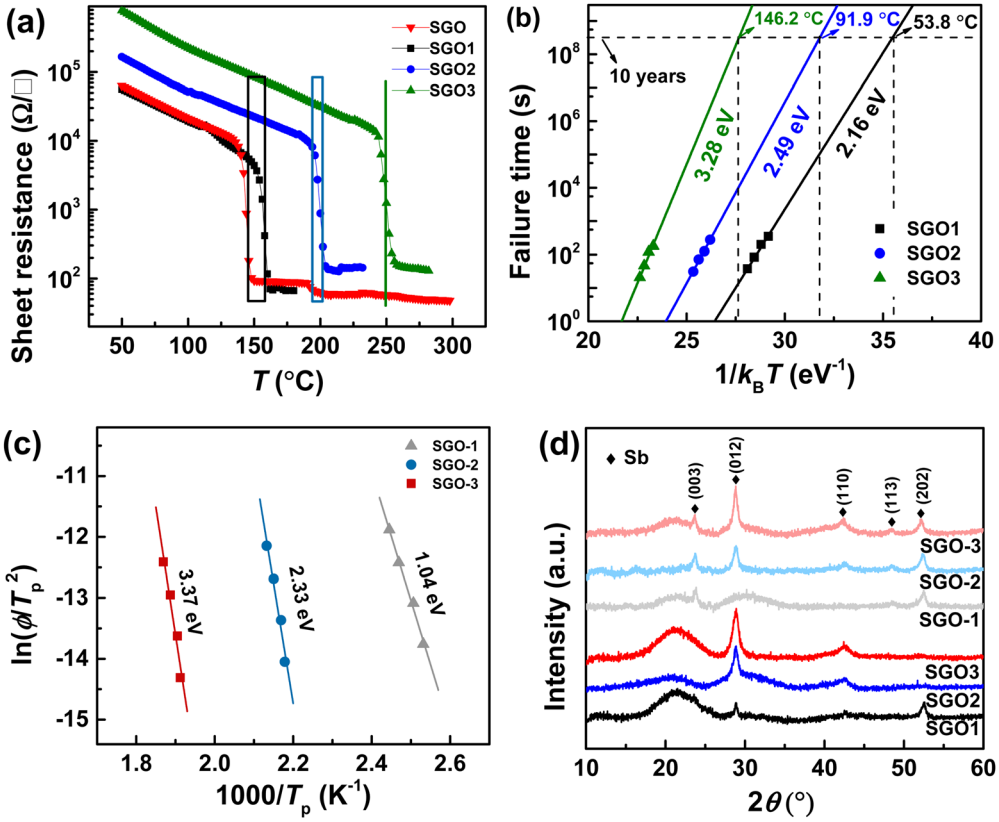

Fig. 3 (a) The temperature-dependent sheet resistances of single SGO films and multilayer SGO film with each phase-change layer is 100 nm. The heating rate is 60 K min^{-1}. (b) The Arrhenius plots of three single SGO films. (c) The Kissinger plots of each SGO phase-change layer in multilayer SGO films. (d) The XRD patterns of crystalline states for single SGO films and each phase-change layer in multilayer SGO film.

(SGO-3), respectively. The larger activation energy for crystallization means that more energy is needed to overcome the barrier to crystallize, implying a better amorphous thermal stability.[26] Compared with the results estimated by the isothermal Arrhenius method and non-isothermal Kissinger method, apparently, the crystallization activation energies of single SGO films are all changed more or less when they are stacked in the multilayer film. In particular, the crystallization activation energy of the SGO-1 layer is significantly smaller than that of the single SGO1 film, indicating that the adjacent phase-change layer in the stacked structure would weaken the amorphous thermal stability distinctly for the phase-change layer with low crystallization temperature.

Fig. 3(d) shows the XRD patterns for the determination of the crystalline phases in SGO films. They are all belong to the Sb crystalline phase (JCPDS no. 1-802) in these SGO films. Besides a weak crystallographic plane (003) that was found, there is no divergence between the crystalline SGO2 and SGO-2 as well as SGO3 and SGO-3. Compared with the crystalline SGO1 and SGO-1, nevertheless, a preferential orientation of crystallographic plane has been detected, *i.e.*, the obvious (012) plane in SGO1 is replaced by the (003) plane in the SGO-1 film. It implies that the amorphous thermal stability and corresponding crystallization behavior of SGO-1 phase-change layer are really influenced by the adjacent layer in the multilayer SGO film.

3.2 Crystallization kinetics features

As we reported in previous studies,[27,28] the SGO film with crystallization temperature of ~200 °C (the SGO2 in this work) exhibits distinct fragility to strong (F–S) crystallization kinetics feature, which is beneficial to balance the contradictory requirement between good amorphous thermal stability (low crystallization rate) around the glass transition temperature (T_g) and fast crystallization rate nearby melting temperature (T_m) in one material. It encourages us to clarify whether F–S crystallization kinetics exists in SGO1 and SGO3 film, and would the adjacent layers influence the crystallization kinetics in multilayer SGO phase-change film? Using the FDSC measurements, we performed the investigations of crystallization kinetics to reveal the above questions. Fig. 4 shows the representative FDSC traces of single and multilayer SGO films. The T_p values of all SGO films increases with the increase in the heating rate. Similar to the results obtained from sheet resistance measurements, only one exothermic peak occurs in the single SGO films but there are three exothermic peaks corresponding to the three-step crystallization, which can be found in the multilayer SGO film.

For discussing the crystallization kinetics quantitatively and more clearly, the above FDSC data are portrayed in the Kissinger plots. The gradient of Kissinger plot indicates the activation energy for crystallization, which can be used for the extrapolation of the crystal growth rate.[29] Fig. 5(a) and (b)

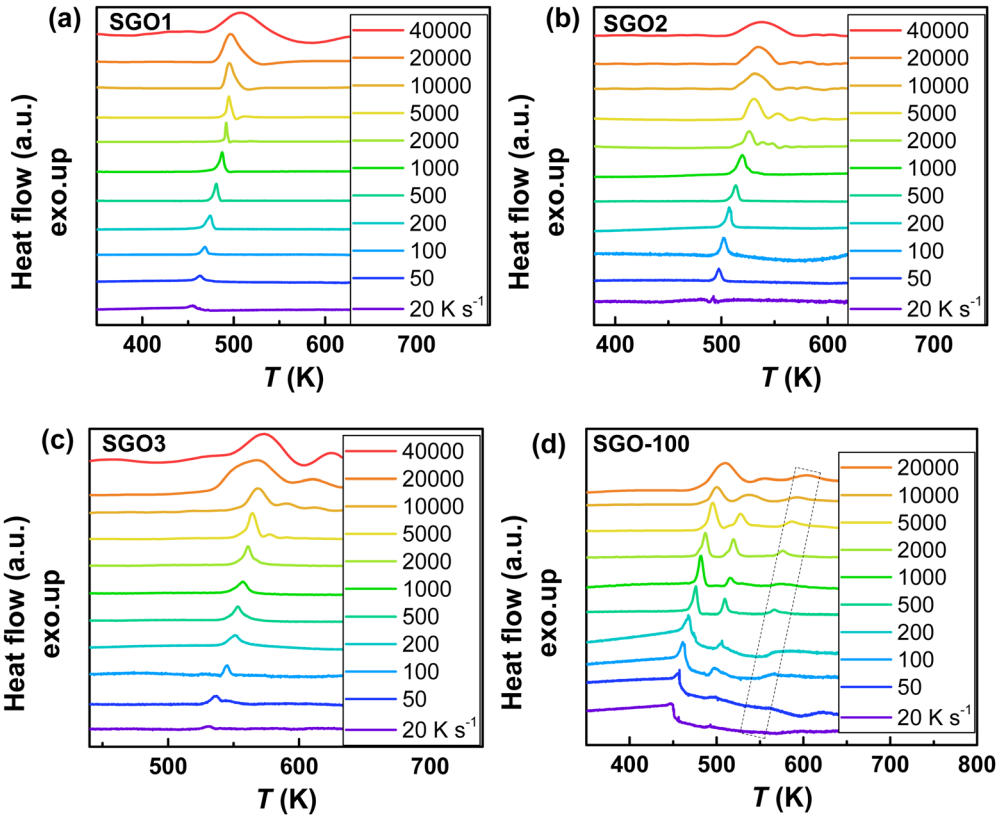

Fig. 4 The representative FDSC traces after background subtraction for (a) SGO1, (b) SGO2, (c) SGO3 single film, and (d) SGO multilayer film. The heating rate is in the range from 20 to 40 000 K s^{-1} for single SGO films, and it is in the range from 20 to 20 000 K s^{-1} for SGO multilayer films. The black dotted zone in Fig. 4(d) represents the relative weak third-order exothermic peak in the SGO multilayer.

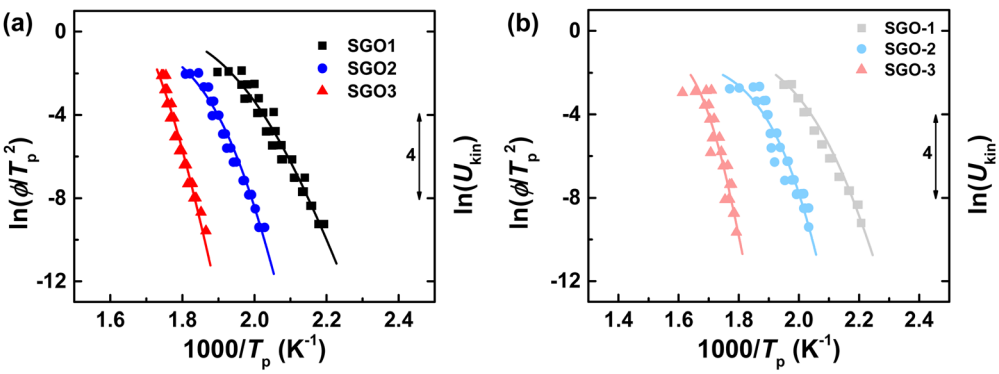

Fig. 5 (a) The Kissinger plots of three single SGO films. (b) The Kissinger plots of each phase-change layer in multilayer SGO film. The related U_{kin} of these SGO films are extrapolated as curved lines using eqn (3).

is the Kissinger plots of single SGO films and multilayer SGO film, respectively. All these plots obey a strict Arrhenius behavior in the low-temperature region, which is similar to the results in Fig. 3(c). However, the non-Arrhenius behaviors are found in these SGO films more or less at the high-temperature region.

Henderson suggested that the Kissinger method could be valid for crystallization kinetics study if the T_p is equal to $T_{0.63}$ (the temperature at which the crystallized fraction is 63%).[30] Due to the unpredictable noise signal in FDSC measurements, the FDSC traces could not be used directly. Before the confirmation, we thus did the JMA numerical simulation, which depends on the T_p values obtained from FDSC traces and combines with the g-MYEGA viscosity model. As we can see in Fig. 6, the T_p values of SGO1 measured by the FDSC traces are perfectly replicated by the JMA numerical simulations. Such numerical simulations of other five SGO films were also performed but are not shown here. There is no obvious divergence

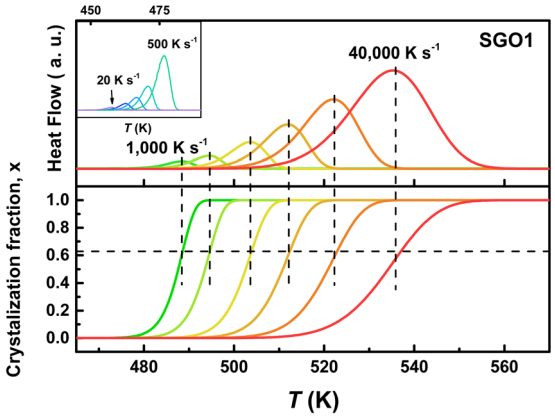

Fig. 6 The JMA numerical simulated FDSC traces (upper layer) and the corresponding crystallized fraction x (bottom layer) of the SGO1 film. The inset in the upper layer depicts the simulated FDSC traces of low heating rates from 20 to 500 K s^{-1}. The horizontal dashed line in the bottom layer indicates the crystallized fraction of 0.63, and the vertical dashed line indicates the T_p at different heating rates.

between T_p and $T_{0.63}$ that can be found even at an ultrahigh heating rate, indicating that the Kissinger method is valid to study the crystallization kinetics in these films. Together with the g-MYEGA viscosity model and Stokes–Einstein relation of $U_{kin} \propto \eta^{-\xi}$ (U_{kin} is the temperature-dependent crystallization kinetics coefficient, η is the temperature-dependent viscosity, ξ is the decoupling coefficient), we then fitted these T_p data and obtained the relative U_{kin} that are the curved lines shown in Fig. 5(a) and (b) using the transposed formula:

$$\log_{10} U_{kin} = C - \xi \times \left\{ \log_{10}\eta_\infty + \frac{1}{T\left[W_1 \exp\left(-\frac{C_1}{T}\right) + W_2 \exp\left(-\frac{C_2}{T}\right)\right]} \right\} \quad (4)$$

where C is the constant to describe the divergence between $\log_{10} U_{kin}$ and $-\log_{10}\eta$, η_∞ is the viscosity at infinite high temperature, W_1 and W_2 are the weight coefficients for the description of brittle phase and the strong phase, and C_1 and C_2 are the two constants corresponding to the two mechanisms of brittleness and strength, respectively.[24] The main fitting parameters are listed in Table 1.

In order to further study the specific impact of the adjacent phase-change layer in stacked multilayer films, we are thus encouraged to further study the temperature-dependent viscosity of these films with the results from the Kissinger plots. The Angell plots, which indicate the change trend of the temperature-dependent viscosity of SGO supercooled liquids, are depicted in Fig. 7(a). Noteworthily, the T_g is determined as the temperature where the η reaches 10^{12} Pa s with the suitable decoupling coefficient ξ used. The T_g is 377, 424, and 476 K for SGO1 (or SGO-1), SGO2 (or SGO-2), and SGO3 (or SGO-3), respectively. As noted here, there is a distinct divergence in the Angell plots of SGO1 and SGO-1, and less divergence in the Angell plots of SGO2 and SGO-2, but almost no divergence in the Angell plots of SGO3 and SGO-3.

Table 1 The main parameters of the Kissinger plot and crystallization kinetics

PCM	W_1	C_1	W_2	C_2	ξ	T_{fs} (K)
SGO1	11062.1	8309.0	0.0099	1524.2	0.79	487
SGO-1	4106.4	7505.7	0.0083	1472.0	0.71	460
SGO2	75123.0	9660.9	0.0038	1374.7	0.81	493
SGO-2	7046.2	8235.5	0.0020	1153.5	0.78	470
SGO3	2.4×10^8	15473.2	0.0622	2911.2	0.73	569
SGO-3	3.3×10^8	15795.3	0.0265	2501.3	0.74	572

The viscosity activation energies of SGO films are estimated in Fig. 7(b). It shows that the E_η of SGO-1 (the gray curve in Fig. 7(b)) increases monotonically as the temperature decrease to T_g, but that of SGO1 increases non-monotonically and reach a plateau at a specific temperature, which is the F–S transition temperature (T_{fs}) and can be calculated by the equation as $T_{fs} = \frac{C_1 - C_2}{\ln W_1 - \ln W_2}$.[31] Such a plateau is also found in other SGO films, indicating the existence of the F–S kinetics feature. However, the introduction of an additional phase-change layer brings an apparent effect on the F–S crystallization kinetics of SGO films. For the low thermal stable SGO1 film, the introduction of additional layers makes the F–S behavior vanish. For the SGO2 film, the F–S temperature T_{fs} decreases from 493 to 470 K as additional layers are introduced. However, for the SGO3 film, the value of T_{fs} is maintained at ~570 K with the introduction of additional layers. Similar to the above obtained results, it is implied that the F–S crystallization kinetics could be influenced significantly when the additional layers capped on the SGO1 film.

3.3 Crystal growth rates

We further estimated the crystal growth rate (U) for these SGO films *via* the formula

$$U = \frac{4 r_{atom} k_B T}{3\pi\lambda^2 R_{hyd} \eta^\xi}\left[1 - \exp\left(-\frac{\Delta G}{k_B T}\right)\right] \quad (5)$$

where r_{atom} is the atomic radius (~1.5 Å), λ is the diffusion jump distance (~1 Å), R_{hyd} is the hydrodynamic radius ($R_{hyd} = r_{atom}$), k_B is the Boltzmann constant of 8.617×10^{-5} eV K^{-1}, η is the temperature-dependent viscosity that has been extrapolated and shown in Fig. 7(a), ξ is the decoupling coefficient that is listed in Table 1, and ΔG is the change in the Gibbs free energy.[32] We here obey the suggestion from Thompson and Spaepen that the ΔG of SGO can be described by the following expression as

$$\Delta G = \frac{\Delta H_m (T_m - T)}{T_m}\left(\frac{2T}{T_m + T}\right) \quad (6)$$

where ΔH_m is the latent heat of melting and T_m is the melting temperature.[33] Taking the above parameters into eqn (4), the temperature-dependent U can be extrapolated. Fig. 8(a) displays a distinct divergence of U (ΔU, more than one order of magnitude) between SGO1 and SGO-1 at low temperature

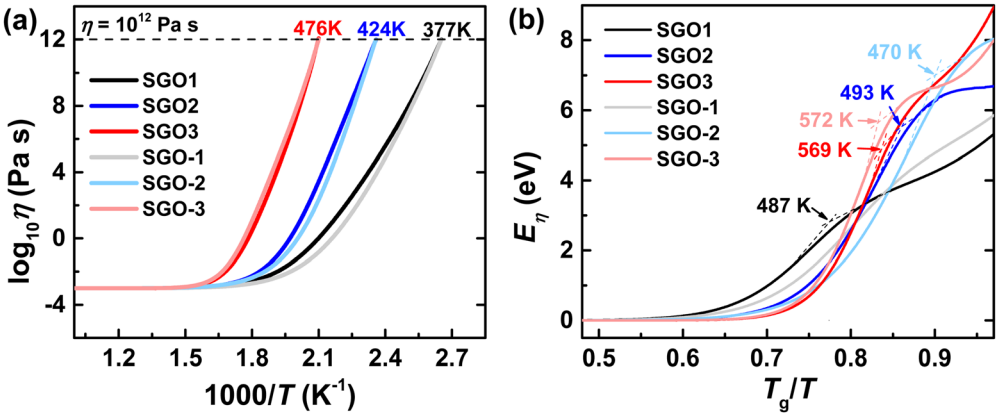

Fig. 7 (a) Angell plots of SGO supercooled liquids. (b) Viscosity activation energy as a function of T_g scaled temperature, $E_\eta = k_B \frac{d\ln(\eta/\eta_0)}{d(1/T)}$, where k_B is the Boltzmann constant of 8.617×10^{-5} eV K^{-1} and η_0 is a fitted parameter.

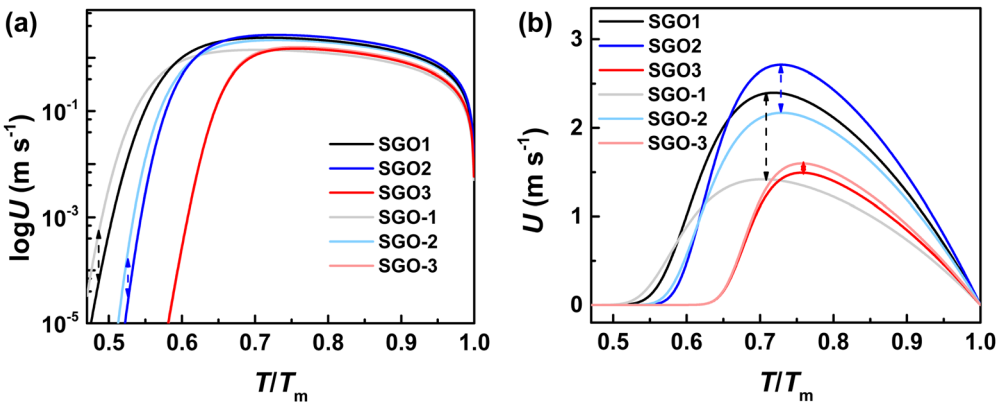

Fig. 8 (a) The logarithmic scale and (b) the linear scale of temperature-dependent crystal growth rate U for SGO films. The dashed arrows indicate the divergences of crystal growth rates between the single SGO film and the SGO layer in the multilayer SGO film.

($\sim 0.5\ T_m$). This divergence is small between SGO2 and SGO-2, but it vanished between SGO3 and SGO-3. From Fig. 8(b), similar results are found in the divergence of U_{max} (ΔU_{max}) at high temperature (0.7–0.8 T_m), *i.e.*, the ΔU_{max} is 1, 0.54, −0.1 m s^{-1} between SGO1 and SGO-1, SGO2 and SGO-2, SGO3 and SGO-3, respectively. It should be figured out that the ΔU_{max} is positive but the ΔU is negative between SGO1 and SGO-1, as well as SGO2 and SGO-2, which is attributed to the F–S kinetics feature that is apparently weakened in the SGO1 and SGO2 films by the introduction of an additional layer.

4. Discussion

It was reported in previous works that the crystallization process of the PCMs would be influenced by the neighboring dielectric layers.[34–37] For instance, Ruitenberg *et al.* found that the nucleation of GST occurs at the interface between the phase-change layer and the dielectric Si_3N_4 layer.[34] Pandian *et al.* found that the nucleation and growth parameters of Sb–Te films were influenced by the dielectric capping layers, such as the activation energy for crystal growth increases 40% as the GeCrN or ZnS–SiO_2 capping layers are added.[35] The above variations observed in the crystallization are attributed to variations in the interface energy between the phase-change layer and the capping layers. However, the decrease of T_p in these SGO films cannot be explained by the interface effect because the 5 nm-thick SiO_2, which is the dielectric layer in the multilayer SGO film, is also capped on the single SGO film. Moreover, the interface effect model based on the amorphous dielectric layer (like the SiO_2 used here) predicts that the introduction of the dielectric layer would hinder crystallization with increased crystallization temperature.[38]

We here consider another reason, which is the stress effect, to deduce the mechanism of the depressed thermal stability in stacked multilayer SGO film. It is well reported that the stress induced can enhance the nucleation or reduce the crystallization temperature.[39] The capping layers would suffer the stresses as high as 1.7 GPa from the GST phase change layer as the shrinkage crystallization happens.[40] Devasia *et al.* analyzed the residual stress in bilayer chalcogenide Ge_2Se_3/SnTe film and found that the amorphous Ge_2Se_3 could also bring continuous stress to impact the crystalline SnTe layer when the temperature increases. The residual stress from the amorphous

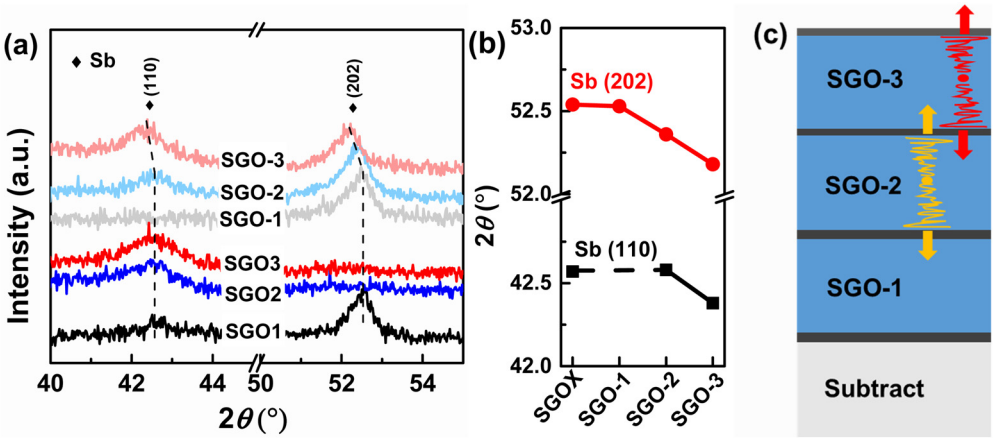

Fig. 9 (a) XRD patterns of SGO film annealed at various temperatures. The SGO1 film and SGO-1 layer in the stacked film are annealed at 170 °C; the SGO2 film and the SGO-2 layer in the stacked film are annealed at 220 °C; the SGO3 film and SGO-3 layer in the stacked film are annealed at 270 °C. (b) The locations of two diffraction peaks in different annealed SGO films and layers. (c) A schematic to describe how the residual stress affects the crystallization of each SGO layer in the stacked films. With the increase in the annealing temperature, the crystallization of low thermal stable SGO-1 layer is affected significantly by the stress from the thermal expansion of the SGO-2 and SGO-3 layer; the crystallization of the SGO-2 layer is slightly affected by the continuous stress from the thermal expansion of SGO-3; the crystallization of the SGO-3 layer is almost unchanged because of the absence of stress arising from the other two phase-change layers as they crystallize.

Ge_2Se_3 layer is more than 1.2 GPa, which results in the SnTe XRD peak shifting significantly.[41]

As shown in Fig. 9(a), which is the enlarged XRD patterns from Fig. 3(d), however, the Sb diffraction peaks can be found to shift significantly with the increase in the annealing temperature. We figured out the diffraction peak shifts of Sb (110) and Sb (202) in Fig. 9(b). As we noted, the Sb (202) plane is present in the crystalline SGO1 film but does not exist in crystalline SGO2 and SGO3. When the stacked multilayer film is annealed at 170 °C (slightly larger than the crystallization temperature of the SGO-1 layer), the Sb (202) plane is also present in the SGO-1 layer. Nevertheless, the corresponding diffraction peak persistently shifts to a low 2θ when the annealing temperature increases to 220 and 270 °C (slightly larger than the crystallization temperature of the SGO-2 and SGO-3 layer, respectively). This implies the large and continuous residual stresses from the SGO2 and SGO3 layer present in the stacked film with the increase in the annealed temperature, and this would be the key factor to affect the crystallization of the SGO1 layer. The Sb (110) plane is present in the SGO2 and SGO3 film but is not apparent in the SGO1 film. This plane is also not found in the SGO-1 layer but detected in the SGO-2 and SGO-3 layer. The corresponding diffraction peak maintains the same position even when the annealing temperature increases to 220 °C, but it shifts to low 2θ as the annealing temperature further increases to 270 °C, indicating that the residual stress from SGO-3 is the essential factor influencing SGO2 crystallization. The schematic to illustrate how the residual stress affects the crystallization behavior of each SGO layer in the stacked films is described in Fig. 9(c). Although there is no evidence to directly confirm where the residual stress comes from this stacked film, we believe the thermal expansion of the SGO layers is the origin.

It is confirmed that the lattice distortions, which are attributed to the residual stress, lead to the above XRD diffraction peak shifts. Together with the XRD results and Bragg's law, we estimated the lattice distortions in the stacked films. The lattice constants (a and c) for rhombohedral Sb were calculated. We chose the stable (003) plane to estimate the value of c as 11.311 Å and then chose the changeable (202) plane to estimate the variational a, which is 3.659, 3.660, 3.670. and 3.683 Å for SGO1, SGO-1, SGO-2, and SGO-3, respectively. In this work, the residual stresses from the SGO phase-change layers are difficult to directly estimate. However, this residual stress from the above lattice distortions can be determined indirectly from a set of interplanar spacings as a function of $\sin^2\Psi$,[42] where Ψ can be the angle difference between the unstressed and stressed film of the diffracting plane. The slope of linear fitting between the interplanar spacing and $\sin^2\Psi$ is calculated as 0.084. The residual stress σ can be determined by $\sigma = mE_f/[a_0(1+\nu_f)]$, where m is the above slope of linear fitting, a_0 is the lattice spacing under the unstressed condition (it is 1.740 Å), and E_f and ν_f are Young's modulus and Poisson's ratio, respectively.[42] The E_f and ν_f of the Sb phase were reported as 6.17×10^{11} dyn cm^{-2} and 0.27, respectively.[43] Taking these parameters in the above equation, the residual stress of the stacked SGO film can be estimated as 2.34 GPa, which is reasonably higher than that of the GST material (1.7 GPa). It implies that the residual stress significantly affects the crystallization behavior of SGO stacked films.

5. Conclusion

We designed a stacked PCM with multistage phase transition. The specific 5 nm thick SiO_2 dielectric layers were introduced into three optimal 100 nm-thick Sb–GeO_2 phase-change layers with the different components of $Sb_{89.2}(GeO_2)_{10.8}$, $Sb_{72.6}(GeO_2)_{27.4}$, and $Sb_{61.8}(GeO_2)_{38.2}$. The multi-level storage with three phase

transitions at the temperatures of 144, 192, and 251 °C, is realized. However, the crystallization temperature, activation energy for crystallization, and crystalline phases of each SGO layer in the multilayer film are changed compared with that of the corresponding single SGO film. Such changes are also observed in their F–S kinetics features, especially in the low thermal stable SGO film, with the introduction of an additional phase-change layers in multilayer films. Based on the analyses from the FDSC data and g-MYEGA viscosity model, it was found that compared with SGO1, the F–S transition temperature T_{fs} and crystal growth rate U of SGO-1 are greatly reduced and that of SGO-2 are slightly changed compared with SGO2, but that of SGO-3 are almost unchanged compared with SGO3. According to the shifts in the crystalline Sb diffraction peaks for these SGO films, we believe that the residual stress comes from the expansion of the additional layers introduced in the stacked multilayer films, which is the natural origin for the changes in the crystallization behaviors and F–S kinetics features. This reveals the influences of additional layers introduced into multilayer films for high-density storage, enabling a systematic optimization of large-scale neuro-inspired computing.

Data availability

The data that support the findings of this study are available from the corresponding authors upon reasonable request.

Conflicts of interest

There are no conflicts to declare.

Acknowledgements

This Project is supported by the National Natural Science Foundation of China (grant no. 62374096, 62075110, 62074089), the Major Program of Zhejiang Provincial Natural Science Foundation of China (LDT23F05012F05), Zhejiang Provincial Natural Science Foundation of China (LY21F040003), the Fundamental Research Funds for the Provincial Universities of Zhejiang (SJLZ2023002), and sponsored by K. C. Wong Magna Fund in Ningbo University, China.

References

1 H. S. P. Wong, S. Raoux, S. Kim, J. Liang, J. P. Reifenberg, B. Rajendran, M. Asheghi and K. E. Goodson, Phase Change Memory, *Proc. IEEE*, 2010, **98**, 2201–2227.
2 G. W. Burr, M. J. Breitwisch, M. Franceschini, D. Garetto, K. Gopalakrishnan, B. Jackson, B. Kurdi, C. Lam, L. A. Lastras, A. Padilla, B. Rajendran, S. Raoux and R. S. Shenoy, Phase change memory technology, *J. Vac. Sci. Technol., B*, 2010, **28**, 223–262.
3 D. Loke, T. H. Lee, W. J. Wang, L. P. Shi, R. Zhao, Y. C. Yeo, T. C. Chong and S. R. Elliott, Breaking the Speed Limits of Phase-Change Memory, *Science*, 2012, **336**, 1566–1569.
4 F. Rao, K. Ding, Y. Zhou, Y. Zheng, M. Xia, S. Lv, Z. Song, S. Feng, I. Ronneberger, R. Mazzarello, W. Zhang and E. Ma, Reducing the stochasticity of crystal nucleation to enable subnanosecond memory writing, *Science*, 2017, **358**, 1423–1426.
5 S. Raoux, W. Welnic and D. Ielmini, Phase Change Materials and Their Application to Nonvolatile Memories, *Chem. Rev.*, 2010, **110**, 240–267.
6 B. Liu, K. Li, W. Liu, J. Zhou, L. Wu, Z. Song, S. R. Elliott and Z. Sun, Multi-level phase-change memory with ultralow power consumption and resistance drift, *Sci. Bull.*, 2021, **66**, 2217–2224.
7 K.-K. Du, Q. Li, Y.-B. Lyu, J.-C. Ding, Y. Lu, Z.-Y. Cheng and M. Qiu, Control over emissivity of zero-static-power thermal emitters based on phase-changing material GST, *Light: Sci. Appl.*, 2016, **6**, e16194.
8 X. Yu, Y. Zhao, C. Li, C. Hu, L. Ma, S. Fan, Y. Zhao, N. Min, S. Tao and Y. Wang, Improved multi-level data storage properties of germanium-antimony-tellurium films by nitrogen doping, *Scr. Mater.*, 2017, **141**, 120–124.
9 Z. Li, Y. Lu, M. Wang, X. Shen, X. Zhang, S. Song and Z. Song, Controllable multilevel resistance state of superlattice-like GaSb/Ge_2Te films for ultralong retention phase-change memory, *J. Non-Cryst. Solids*, 2018, **481**, 110–115.
10 A. I. Khan, H. Kwon, M. E. Chen, M. Asheghi, H. S. P. Wong, K. E. Goodson and E. Pop, Electro-Thermal Confinement Enables Improved Superlattice Phase Change Memory, *IEEE Electron Device Lett.*, 2022, **43**, 204–207.
11 R. Liu, P. Wu, Z. He, J. Zhai, X. Liu and T. Lai, Study of crystallization and thermal stability of superlattice-like $SnSb_4$-GeTe thin films, *Thin Solid Films*, 2017, **625**, 11–16.
12 W. Wu, S. Chen, J. Zhai, X. Liu, T. Lai, S. Song and Z. Song, Multi-level storage and ultra-high speed of superlattice-like $Ge_{50}Te_{50}/Ge_8Sb_{92}$ thin film for phase-change memory application, *Nanotechnology*, 2017, **28**, 405206.
13 Y. Hu, X. Feng, S. Li, T. Lai, S. Song, Z. Song and J. Zhai, Superlattice-like $Sb_{50}Se_{50}/Ga_{30}Sb_{70}$ thin films for high-speed and high density phase change memory application, *Appl. Phys. Lett.*, 2013, **103**, 152107.
14 K. Jiang, Y. Lu, Z. Li, M. Wang, X. Shen, G. Wang, S. Song and Z. Song, GeTe/Sb_4Te films: A candidate for multilevel phase change memory, *Mater. Sci. Eng., B*, 2018, **231**, 81–85.
15 Y. G. Liu, Y. F. Chen, D. L. Cai, Y. Y. Lu, L. Wu, S. Yan, Y. Li, J. J. Lu, L. Yu and Z. T. Song, High performance of multilevel-cell phase change memory device with good endurance reliability, *Semicond. Sci. Technol.*, 2019, **34**, 105019.
16 M. S. Arjunan, A. Mondal, S. Durai, K. V. Adarsh and A. Manivannan, Impact of crystallization process in multilevel optical switching in $Ge_2Sb_2Te_5$ and $Ag_5In_5Sb_{60}Te_{30}$ phase-change materials, *J. Phys. D: Appl. Phys.*, 2020, **53**, 495303.
17 Y. Chen, H. Pan, S. Mu, G. Wang, R. Wang, X. Shen, J. Wang, S. Dai and T. Xu, Intermediate crystallization kinetics in Germanium-Tellurides, *Acta Mater.*, 2019, **164**, 473–480.
18 C. Zhang, L. Hu, Y. Yue and J. C. Mauro, Fragile-to-strong transition in metallic glass-forming liquids, *J. Chem. Phys.*, 2010, **133**, 014508.

19 W. A. Johnson and R. F. Mehl, Reaction kinetics in processes of nucleation and growth, *Trans. AIME*, 1939, **135**, 396–415.
20 M. Avrami, Kinetics of Phase Change. I General Theory, *J. Chem. Phys.*, 1939, **122**, 064901.
21 M. Avrami, Kinetics of phase change. II transformation-time relations for random distribution of nuclei, *J. Chem. Phys.*, 1940, **122**, 064901.
22 M. Avrami, Granulation, phase change, and microstructure kinetics of phase change. III, *J. Chem. Phys.*, 1941, **122**, 064901.
23 W. Zhang and E. Ma, Unveiling the structural origin to control resistance drift in phase-change memory materials, *Mater. Today*, 2020, **41**, 156–176.
24 Y. Chen, J. Gu, Q. Zhang, Y. Mao, G. Wang, R. Wang, X. Shen, J.-Q. Wang and T. Xu, Fragile-to-strong crossover in optimized In-Sb-Te phase-change supercooled liquids, *Phys. Rev. Mater.*, 2020, **4**(3), 033403.
25 B. Chen, G. H. ten Brink, G. Palasantzas and B. J. Kooi, Crystallization kinetics of GeSbTe phase-change nanoparticles resolved by ultrafast calorimetry, *J. Phys. Chem. C*, 2017, **121**, 8569–8578.
26 G. Wang, F. Liu, Y. Lu, Y. Chen and X. Shen, Crystallization mechanism and switching behavior of In-S-Sb phase change thin films, *Appl. Phys. Lett.*, 2021, **119**, 011601.
27 K. Peng, Y. Chen, W. Leng, G. Wang, C. Gu, Y. Gao, J.-Q. Wang and X. Shen, Tailorable fragile-to-strong kinetics features of metal oxides nanocomposite phase-change antimony films, *Acta Mater.*, 2022, **234**, 118013.
28 K. Peng, Y. Chen, Y. Meng, J.-Q. Wang, C. Gu, Y. Gao, G. Wang and X. Shen, Revealing the influence of oxygen doping on the crystallization kinetics of Sb–GeO_2, *Cryst. Growth Des.*, 2022, **22**, 4970–4976.
29 J. Orava, D. W. Hewak and A. L. Greer, Fragile-to-strong crossover in supercooled liquid Ag–In–Sb–Te studied by ultrafast calorimetry, *Adv. Funct. Mater.*, 2015, **25**, 4851–4858.
30 D. W. Henderson, Thermal analysis of non-isothermal crystallization kinetics in glass forming liquids.pdf, *J. Non-Cryst. Solids*, 1979, **30**, 301–315.
31 C. Zhou, L. N. Hu, Q. J. Sun, H. J. Zheng, C. Z. Zhang and Y. Z. Yue, Structural evolution during fragile-to-strong transition in CuZr(Al) glass-forming liquids, *J. Chem. Phys.*, 2015, **142**, 064508.
32 M. Salinga, E. Carria, A. Kaldenbach, M. Bornhofft, J. Benke, J. Mayer and M. Wuttig, Measurement of crystal growth velocity in a melt-quenched phase-change material, *Nat. Commun.*, 2013, **4**, 2371.
33 C. A. Angell, Glass formation and glass transition in supercooled liquids, with insights from study of related phenomena in crystals, *J. Non-Cryst. Solids*, 2008, **354**, 4703–4712.
34 G. Ruitenberg, A. K. Petford-Long and R. C. Doole, Determination of the isothermal nucleation and growth parameters for the crystallization of thin $Ge_2Sb_2Te_5$ films, *J. Appl. Phys.*, 2002, **92**, 3116–3123.
35 R. Pandian, B. J. Kooi, J. T. M. De Hosson and A. Pauza, Influence of capping layers on the crystallization of doped Sb_xTe fast-growth phase-change films, *J. Appl. Phys.*, 2006, **100**, 123511.
36 W. K. Njoroge, H. Dieker and M. Wuttig, Influence of dielectric capping layers on the crystallization kinetics of $Ag_5In_6Sb_{59}Te_{30}$ films, *J. Appl. Phys.*, 2004, **96**, 2624–2627.
37 R. Berthier, N. Bernier, D. Cooper, C. Sabbione, F. Hippert and P. Noe, In situ observation of the impact of surface oxidation on the crystallization mechanism of GeTe phase-change thin films by scanning transmission electron microscopy, *J. Appl. Phys.*, 2017, **122**, 115304.
38 M. Zacharias and P. Streitenberger, Crystallization of amorphous superlattices in the limit of ultrathin films with oxide interfaces, *Phys. Rev. B: Condens. Matter Mater. Phys.*, 2000, **62**, 8391–8396.
39 Y. P. Mitrofanov, M. Peterlechner, I. Binkowski, M. Y. Zadorozhnyy, I. S. Golovin, S. V. Divinski and G. Wilde, The impact of elastic and plastic strain on relaxation and crystallization of Pd–Ni–P-based bulk metallic glasses, *Acta Mater.*, 2015, **90**, 318–329.
40 T. P. L. Pedersen, J. Kalb, W. K. Njoroge, D. Wamwangi, M. Wuttig and F. Spaepen, Mechanical stresses upon crystallization in phase change materials, *Appl. Phys. Lett.*, 2001, **79**, 3597–3599.
41 A. Devasia, F. Bai, M. Davis, K. A. Campbell, S. Gupta and S. Kurinec, Analyzing residual stress in bilayer chalcogenide Ge_2Se_3/SnTe films, *Thin Solid Films*, 2009, **517**, 6516–6519.
42 R. Wang, S. Pan and Y. Zhou, Stress reduction by ion bombardment in CeO_2 films, *Solid State Commun.*, 2000, **114**, 613–616.
43 D. J. Gunton and G. A. Saunders, The Young's modulus and Poisson's ratio of arsenic, antimony and bismuth, *J. Mater. Sci.*, 1972, **7**, 1061–1068.